Chalcogenide Letters Vol. 22, No. 9, September 2025, p. 777 - 785

ZnO/ZnS sensor with broadband visible response for flexible polyethylene terephthalate substrates combined with artificial intelligence analysis

X. Y. Chen [a,b], Y. H. Cai [a], Y. S. Chen [c], S. J. Huang [b], M. H. Li [d], Y. H. Li [e], C. H. Lin [c], H. Chen [a,*]

[a] *Department of Applied Materials and Optoelectronic Engineering, National Chi Nan University, Puli 54561, Taiwan ROC*

[b] *Department of Mechanical Engineering, National Taiwan University of Science and Technology, Taipei 10607, Taiwan ROC*

[c] *Department of Photonics, National Cheng Kung University, Tainan 70101, Taiwan ROC*

[d] *Department of Optoelectronic Engineering, National Formosa University, Yunlin 63201, Taiwan ROC*

[e] *AI Research Center, Hon Hai Research Institute, 11494, Taipei, Taiwan ROC*

This study focuses on the development of zinc oxide (ZnO)/zinc sulfide (ZnS) core-shell structures on flexible polyethylene terephthalate (PET) substrates for enhanced light sensing. PET offers high elasticity, optical transparency, and chemical resistance, making it ideal for wearable optoelectronics. By optimizing the vulcanization process, a uniform ZnS shell is formed on the exposed regions of ZnO nanorods (NRs), significantly enhancing ZnO-based sensor's sensitivity to visible light, especially red light (peak wavelength at 630 nm). Structural and spectral analyses confirm the successful formation of the ZnO/ZnS heterostructure, improved charge separation, and broadened light response. To improve data processing and classification accuracy, a one-dimensional convolutional neural network (1D-CNN) is applied to analyze the time-series signals from the sensor. The model achieves 100% training accuracy and nearly perfect performance on the test set, as shown in the confusion matrices. This demonstrates strong generalization and stable classification across different light conditions. The integration of nanomaterial engineering and AI-assisted analysis highlights a promising strategy for future development of intelligent, flexible, and high-performance optical sensing systems.

(Received June 29, 2025; Accepted September 7, 2025)

Keywords: Flexible substrates, Photosensitive, Vulcanization, Heterostructure, Visible light

1. Introduction

In recent years, flexible optoelectronic devices have gained significant attention due to their potential applications in wearable electronics, environmental monitoring, and the Internet of Things (IoT)[1, 2]. Among various sensor technologies, visible-light photodetectors play a critical role in converting optical signals into electrical data, enabling real-time monitoring and intelligent response systems. This study focuses on the development of a flexible photodetector based on a zinc oxide (ZnO)/zinc sulfide (ZnS) core-shell nanostructure[3, 4] grown on a polyethylene terephthalate (PET) substrate[5, 6], aimed at enhancing mechanical flexibility and extending device applicability in dynamic or curved environments.

ZnO is a widely studied n-type semiconductor[7-9] with a wide bandgap (3.37 eV), high electron mobility, excellent chemical stability, and strong exciton binding energy (60 meV), making it ideal for UV-light detection. However, its limited visible-light absorption remains a major challenge for broader sensing applications. To address this, a ZnS shell, which has a slightly

* Corresponding author: hchen@ncnu.edu.tw

https://doi.org/10.15251/CL.2025.229.777

narrower bandgap (~3.6 eV) and high optical stability[10], is introduced to form a ZnO/ZnS core-shell heterojunction. This configuration enhances photogenerated carrier separation[11] and extends the photo response into the visible spectrum[12], significantly improving the photodetection performance.

To further optimize the device, the thickness of the ZnS shell and sulfurization conditions were carefully controlled to balance structural integrity with interfacial efficiency. Additionally, a deep learning model based on convolutional neural networks (CNN) was implemented in MATLAB to extract and classify waveform features from sensor outputs, providing higher accuracy and reliability in complex environments.

Overall, the integration of a ZnO/ZnS heterojunction with a flexible PET substrate, combined with AI-driven signal analysis, establishes a versatile platform for next-generation smart optoelectronic devices, with promising applications in flexible photodetectors and wearable electronics.

2. Experimental section

In this study, a ZnO seed layer was spin-coated on a PET substrate on which an interdigitated electrode had been deposited. Subsequently, ZnO nanorods (NRs) are grown by chemical bath deposition (CBD). After completing the growth of the nanorods, the material is further vulcanized by CBD using sodium sulfide (Na_2S) to induce the formation of a ZnS/ZnO core-shell structure. In order to optimize the material properties and sensing performance, the curing time was systematically adjusted to 5, 10, 15, and 20 minutes to select the samples with the best structure and performance. Subsequently, the devices were subjected to optical sensing performance tests and electrical measurements to evaluate their sensing behaviors and electrical changes under different vulcanization conditions. At the same time, through physical structure analysis and chemical composition identification, the influence of microstructure and elemental distribution on the photoelectric properties of the materials is investigated in depth.

3. Results and discussion

The surface morphology of the samples was analyzed using a dual beam focused ion beam (DB-FIB) system, which integrates both focused ion beam (FIB) and scanning electron microscope (SEM) functions to provide high-resolution nanoscale imaging. As shown in Fig. 1(a), the as-grown ZnO NRs are densely packed, vertically aligned, and exhibit a uniform, smooth surface. After 5 minutes of vulcanization, a thin ZnS shell begins to form, as seen in Fig. 1(b), with slight surface roughening while the ZnO structure remains largely intact. At 10 minutes, the ZnS shell uniformly covers the nanorods Fig. 1(c), enhancing surface roughness and forming a well-defined core-shell structure. In contrast, excessive growth is observed at 15 and 20 minutes, as respectively seen in Fig. 1(d) and Fig. 1(e), leading to aggregation and irregular morphology that may affect device stability. Among all, the 10-minute treatment offers the best balance between structural order and performance.

Despite slight deformation of the PET substrate during growth, high-resolution transmission electron microscopy (HRTEM) analysis in Fig. 1(f) shows that the ZnS shell presents a clear and regular lattice, indicating good crystallinity. The ZnO–ZnS interface is sharp and distinct, with no evidence of interfacial diffusion or structural defects, confirming that the core-shell heterostructure maintains excellent crystallization quality and integrity even when grown on a flexible substrate.

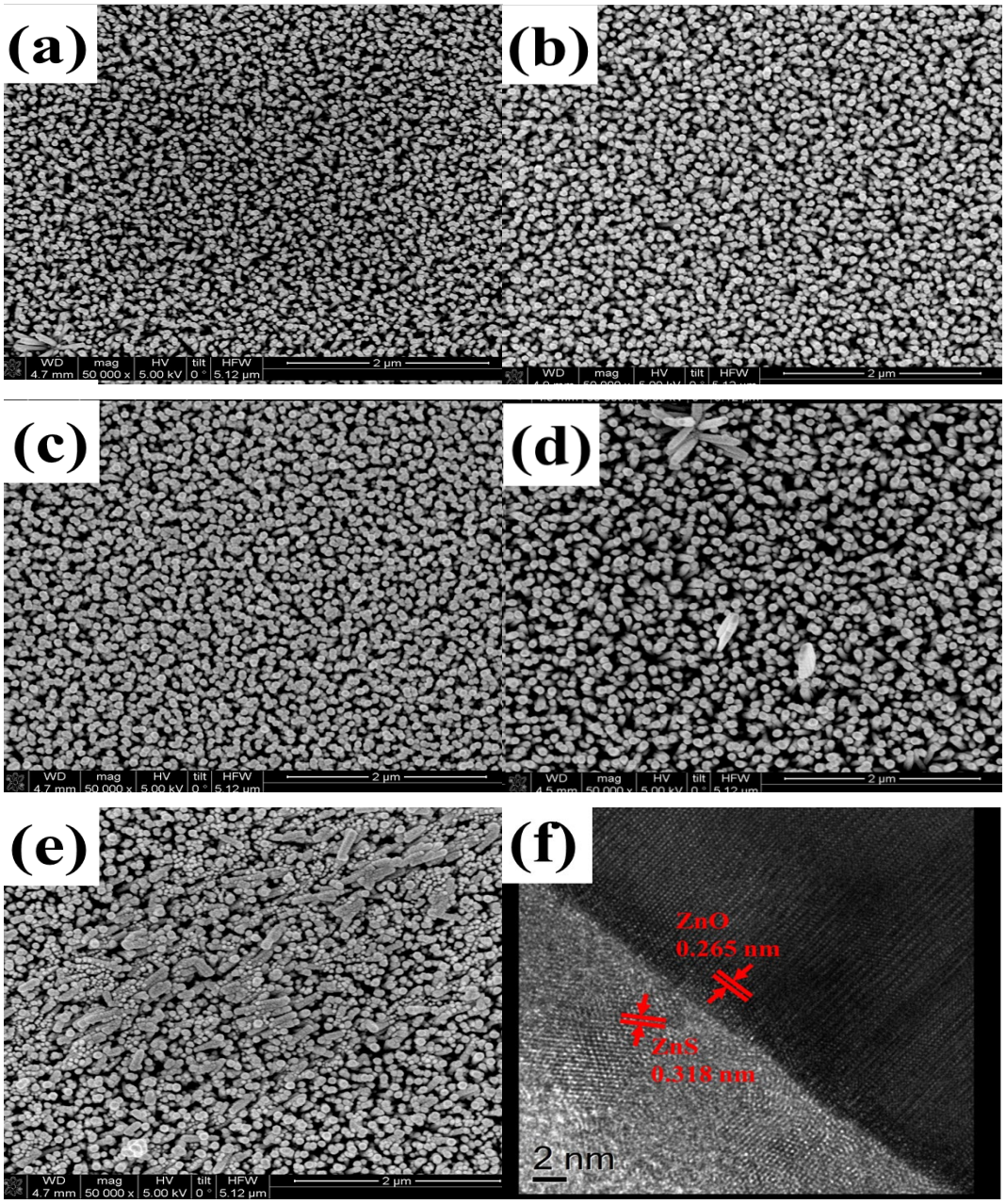

Fig. 1. Top-view SEM images of ZnO nanorods treated with different vulcanization times: (a) 0 min (pristine ZnO), (b) 5 min, (c) 10 min, (d) 15 min, and (e) 20 min. (f) TEM image of ZnO/ZnS heterojunction (vulcanization time of 10 min).

X-ray diffraction (XRD) analysis, as shown in Fig. 2(a), confirms that the ZnO nanostructures grown on PET substrates exhibit a typical hexagonal wurtzite structure, with prominent diffraction peaks observed at 31.8° ((100) facet), 34.4° ((002) facet), 36.3° ((101) facet), 47.5° ((102) facet), and 62.9° ((103) facet), indicating excellent crystallinity. After sulfurization, additional peaks appear at 33.1° ((200) facet) and 47.5° ((220) facet), corresponding to the cubic ZnS phase. The increasing ZnS signal intensity with prolonged treatment suggests progressive shell formation, while the ZnO peaks remain stable, confirming the preservation of the core-shell structure.

According to the quantitative EDS analysis, the pristine ZnO sample contains 36.44 wt% Zn and 6.01 wt% O, with no detectable sulfur signal, as shown in Fig. 2(b). In contrast, in Fig. 2(c), the ZnO/ZnS core–shell sample exhibits an additional S peak, with 52.17 wt% Zn, 13.38 wt% O,

and 9.50 wt% S. After excluding the carbon background and renormalizing, the composition of the core–shell sample corresponds to ~69.5 wt% Zn, 17.8 wt% O, and 12.7 wt% S, giving an S/Zn weight ratio of ~0.18. The relatively low sulfur content and the preservation of a strong Zn signal confirm that the ZnS shell forms only a thin surface layer rather than a thick overlayer. Together with the XRD results, these findings demonstrate that moderate sulfurization produces a well-defined ZnO/ZnS core–shell heterostructure with good interfacial definition and minimal disturbance to the ZnO core crystallinity.

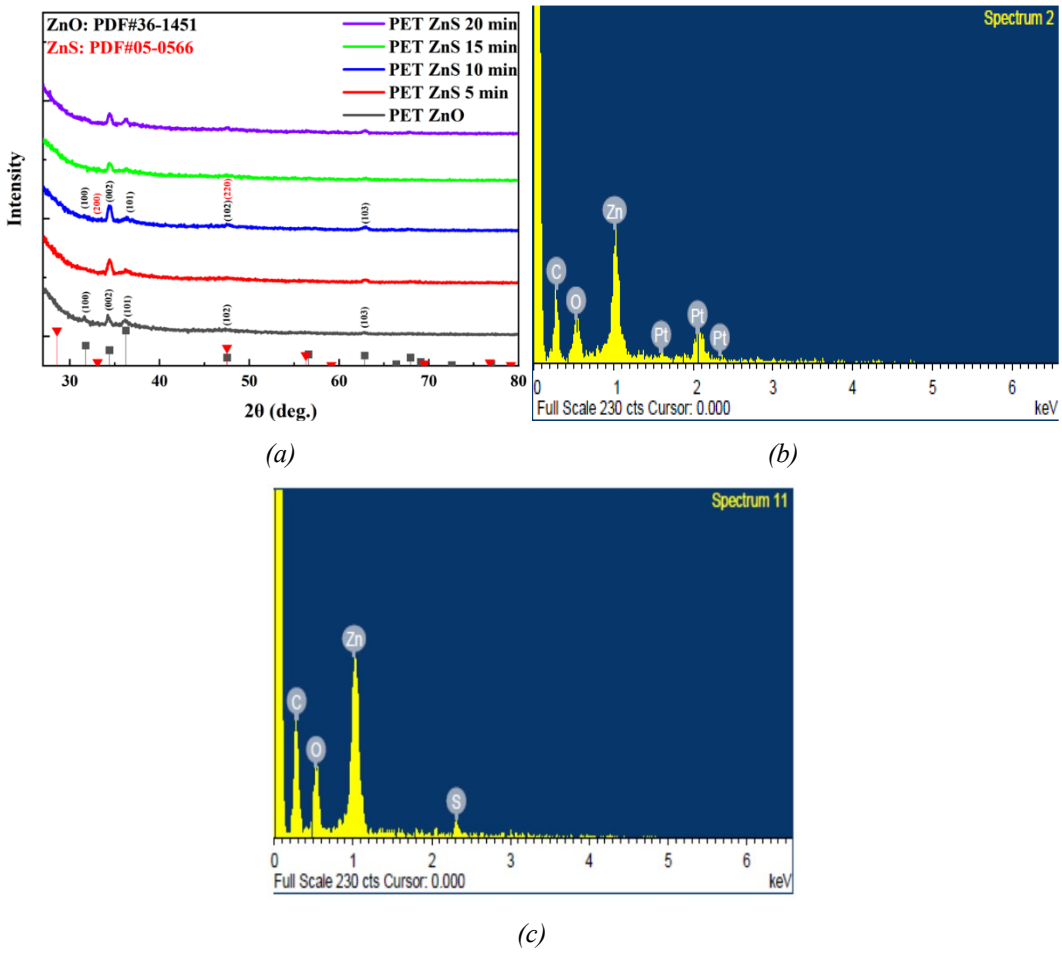

(a) *(b)*

(c)

Fig. 2. (a) XRD patterns of ZnO/ZnS nanostructures on PET substrates with different sulfurization times, showing the characteristic peaks of ZnO (PDF#36-1451) and ZnS (PDF#05-0566) and confirming progressive shell formation. (b) EDS spectrum of pristine ZnO displaying only Zn and O signals. (c) EDS spectrum of ZnO/ZnS core–shell structures showing an additional S peak, with its relatively low intensity indicating that the ZnS forms a thin shell layer rather than a thick overlayer.

Photoluminescence (PL) spectra shown in Fig. 3(a) reveal the evolution of optical properties and defect states in ZnO/ZnS heterostructures. Unsulfurized ZnO sample exhibits a broad emission around 400 nm, slightly red-shifted from the typical ZnO near-band-edge (360–380 nm), likely due to surface defects, lattice strain, and poor crystallinity on PET substrates. After 5 min of sulfurization, the PL emission intensity at ~400 nm slightly increases, while longer treatments lead to a blue-shift and decreased PL intensity, indicating that the ZnS shell effectively passivates surface defects and restores near-band-edge emission.

Additionally, visible broadband emission (500–700 nm) becomes more pronounced after sulfurization, especially in the 10 min sample. This enhancement is attributed to deep-level defect states and carrier recombination at the ZnO/ZnS interface, where band offsets promote charge separation and radiative recombination.

In Fig. 3(b), Raman spectra support these findings. A strong ZnO peak at ~573 cm^{-1} (E_2 high mode) weakens and broadens after sulfurization, indicating surface lattice disturbance. Meanwhile, a new ZnS-related peak at ~350 cm^{-1} emerges, confirming shell formation. The 10-min treated sample shows balanced and distinct peaks from both ZnO and ZnS, reflecting good crystallinity and interfacial quality, making it the most optimal sulfurization condition.

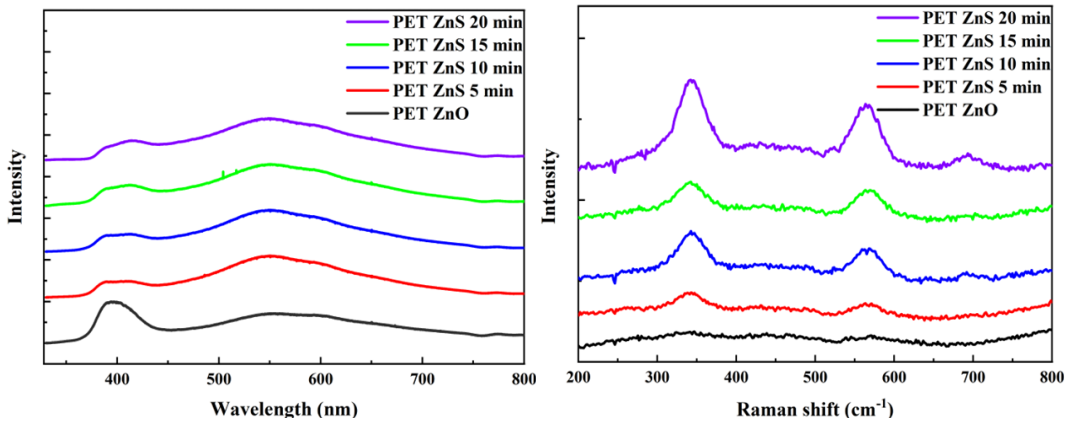

Fig. 3. (a) PL spectra of ZnO NRs treated with different vulcanization times, showing enhanced visible emission and defect passivation after sulfurization, with 10 min being optimal. (b) Raman spectra of ZnO NRs treated with different vulcanization times confirm ZnS formation (~350 cm^{-1}) and reduced ZnO crystallinity (~573 cm^{-1}) with increased sulfurization time.

Figure 4 presents the current-time (I-t) curves of ZnO- and ZnO/ZnS-based devices that under consecutive on/off red, green, blue, and UV LEDs illuminations. The ZnO NRs-based device without sulfurization shows minimal photoelectric response to blue, green, and red LEDs illumination, with little current variation, reflecting its wide bandgap limitation in the visible spectrum. In contrast, the devices using ZnO/ZnS core-shell structure significant photoresponse, indicating improved carrier separation and heterojunction effects.

Sensitivity (**S**) was calculated as $S = (I_{Light} - I_{dark})/I_{dark}$, where I_{dark} and I_{Light} are the steady-state currents under illumination and dark conditions, respectively. The photoresponsivity (**R**) was determined from $R = (I_{Light} - I_{dark})/P_{opt} \times Area$, where P_{opt} is the incident optical power. Rise and recovery times were extracted as the durations required for the current to reach 90 % of its final value upon light-on and drop to 10 % after light-off.

When exposed to red LED, the ZnO/ZnS-based device exhibits a sensitivity of 5.814 and a responsivity of 0.109, with rise and recovery times of 21.53 and 20.23 seconds, respectively. However, the response waveform remains unstable, likely due to uneven shell coverage, surface roughness, and crystal defects.

In the case of green light, the structure reaches a sensitivity of 19.549 and a responsivity of 3.799. Rise and recovery times are 20.80 and 20.54 seconds, respectively, yet the waveform shows persistent instability, including frequent noise and sharp peaks. These issues reflect suboptimal crystal quality, as confirmed by SEM and Raman analysis.

Exposure to blue light results in a sensitivity of 323.485 and a notably higher responsivity of 30.133. The corresponding rise and recovery times decrease to 4.16 and 4.38 seconds. Despite the faster response, the signal remains noisy and unstable, likely due to surface irregularities and inconsistent shell formation.

Under UV illumination, the ZnO/ZnS-based device demonstrates significantly enhanced performance, achieving a sensitivity of 726.48 and a responsivity of 2680.11. Rise and recovery times are sharply reduced to 1.69 and 1.13 seconds, respectively. Strong UV emission observed in PL spectra and well-defined Raman peaks confirm uniform shell coverage and efficient UV sensing behavior.

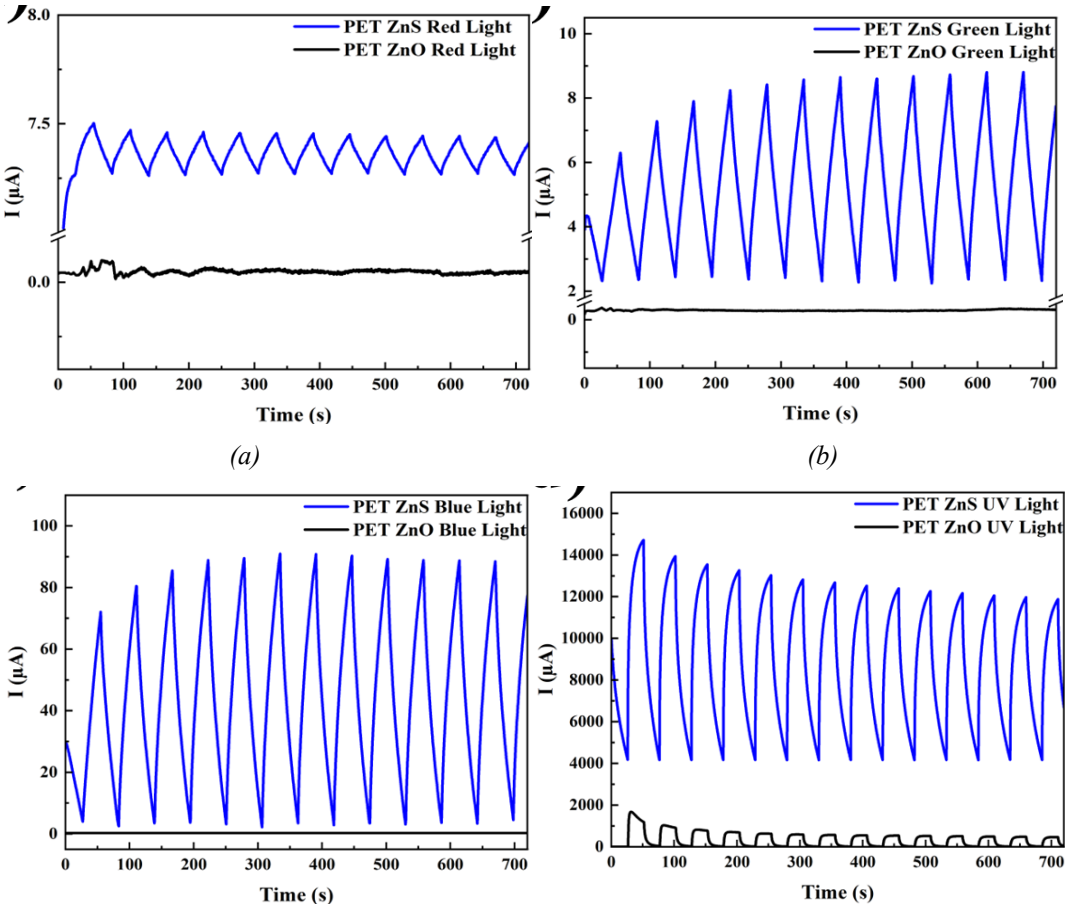

Fig. 4. Time dependent photoresponse curves of PET-based ZnO and ZnS structures under (a) red, (b) green, (c) blue, and (d) UV LEDs illumination. ZnS structures show significantly higher photocurrents and clearer switching responses.

The I-t response curves of the ZnO/ZnS-based sensors under red LED illumination for various bending conditions are presented in Fig. 5(a). Notably, the baseline dark current remained consistently low at approximately 0.001 μA across all measurements. For the bending tests, we used molds with fixed curvature, as shown in Fig. 5(b). During the I-t measurements, devices were mounted on a mold, with the sensing area highlighted in yellow, as illustrated in Fig. 5(c). A photograph of the device mounted on the mold is provided in Fig. 5(d). The unbent sample exhibited the highest average current of approximately 2.6317 μA, yielding a sensitivity of 262.17 and a responsivity of 0.101. As bending curvature was increased (from bending 1 with a mold height of 10 cm to the most extreme bending 7 with a mold height of 34 cm), Fig. 5(a) reveals a gradual decline in both sensitivity and responsivity. Under the most extreme bending condition, these values dropped significantly to 3.406 and 0.0013, respectively. This substantial performance degradation is probably attributed to structural strain and potential microcracking within the device.

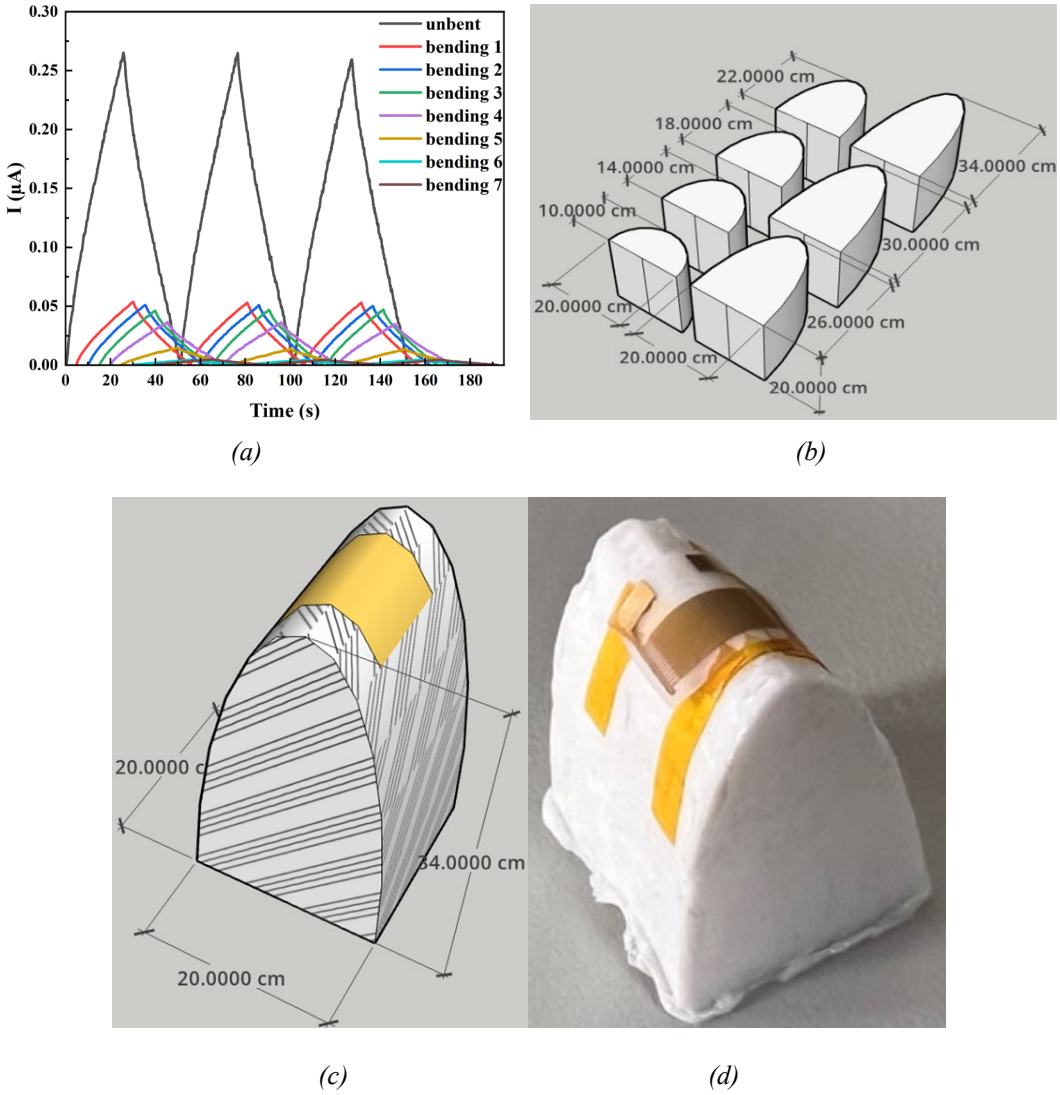

(a) *(b)*

(c) *(d)*

Fig. 5 (a) Time dependent current response of ZnO/ZnS-based devices under different bending conditions. (b) Illustration of bending models with fixed radius (1.0 cm to 3.4 cm) for bending test. (c) Illustration and (d) photograph of flexible device mounted on a single bending model.

To enhance the classification efficiency and accuracy of light sensor data, this study utilizes a one-dimensional convolutional neural network (1D-CNN) as the primary recognition model. Given that light sensor outputs are time-series I-t signals, the 1D-CNN effectively captures temporal features and characteristic trends, enabling precise identification under varying light and bending conditions. Before training, raw data undergoes preprocessing, including noise removal, signal normalization, and segmentation into fixed-size overlapping windows, each labeled with the corresponding light source to ensure consistent learning.

The classification results are summarized in the confusion matrices shown in Fig. 6. The training set matrix in Fig. 6 (a) demonstrates perfect classification, with each light type (UV, blue, green, and red LEDs) achievingA 100% accuracy, correctly identifying all 40 samples without misclassification. In the test set in Fig. 6 (b), the model maintains high accuracy, correctly classifying 157 UV, 157 Blue, 157 Green, and 156 Red light samples, reflecting strong generalization and reliable performance across diverse optical inputs.

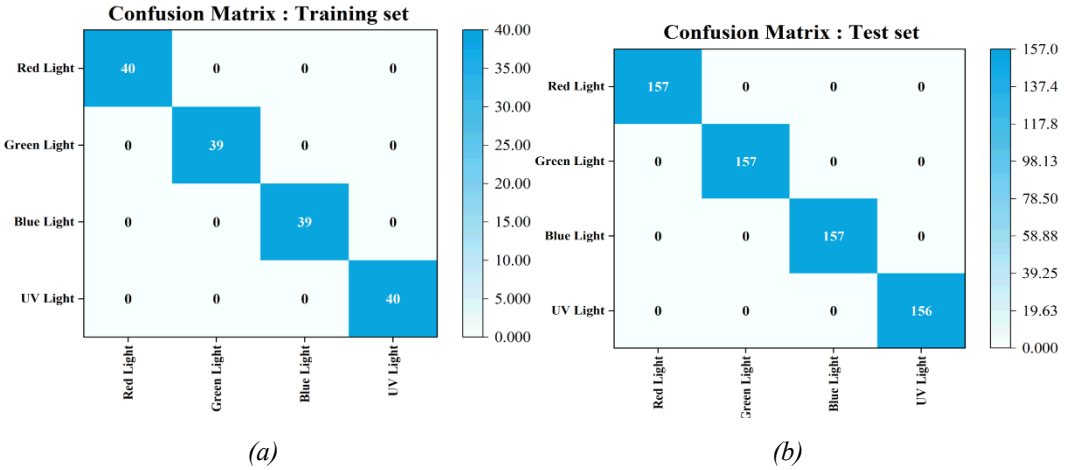

Fig. 6. Confusion matrices for PET-based sensors under different light sources, showing classification performance for four illumination conditions: (a) Training set, and (b) test set.

4. Conclusions

This study successfully fabricated ZnO/ZnS core-shell structures with enhanced optical detection performance. By optimizing the sulfurization process at 10 minutes, well-defined ZnO/ZnS structures were constructed on flexible PET substrates, showing significantly improved light sensing capability. A combination of SEM, TEM, XRD, PL, and Raman techniques was used to verify the structure and properties in detail. AI-assisted analysis was also applied to identify sensing waveforms, confirming the potential of ZnO/ZnS core-shell structures on PET substrates. The results show that ZnO/ZnS heterostructures outperform ZnO in the visible light range, laying a solid foundation for the development of flexible wearable devices and light-sensing systems in the Internet of Things.

Furthermore, the application of a CNN for time-series signal classification demonstrated excellent accuracy and generalization, validating the effectiveness of AI in enhancing sensor performance and data interpretation. This integration of advanced materials with AI-driven analysis paves the way for intelligent and high-efficiency optoelectronic sensing platforms.

Acknowledgements

We gratefully acknowledge the financial support provided by the National Science and Technology Council (NSTC) under project NSTC 113-2221-E-260-005. We also appreciate the valuable assistance from various analytical laboratories for their support in material characterization and data analysis, which were essential for the successful completion of this research.

Special thanks to Dr. Guang-Guo Wang, a postdoctoral researcher, for his support in high-resolution field emission scanning transmission electron microscopy (HR-FE-STEM) analysis. This advanced instrument, operating at 80-200 kV, is suitable for a wide range of materials, including metals, semiconductors, ceramics, biomaterials, polymers, metal-organic frameworks (MOFs), and electron beam-sensitive nanomaterials. It offers high-resolution imaging in both TEM and STEM modes, microdiffraction, atomic-scale EDS, chemical mapping, line profile analysis, and 3D stereoscopic imaging, providing critical insights into the morphology, structure, and elemental composition of nanomaterials.

References

[1] Peng, M., Z. Wen, X. Sun, Advanced Functional Materials, 2023. 33(11): p. 2211548; https://doi.org/10.1002/adfm.202211548

[2] Yoo, H., et al., Advanced Materials, 2021. 33(47): p. 2006091; https://doi.org/10.1002/adma.202006091

[3] Benyahia, K., et al., Journal of Alloys and Compounds, 2021. 859: p. 158242; https://doi.org/10.1016/j.jallcom.2020.158242

[4] Suguna, A., et al., Journal of Materials Science: Materials in Electronics, 2023. 34(23): p. 1655; https://doi.org/10.1007/s10854-023-11059-5

[5] Tran, M.H., J. Hur, EcoMat, 2023. 5(3): p. e12301; https://doi.org/10.1002/eom2.12301

[6] Pavelyev, V., et al., Journal of Materials Science: Materials in Electronics, 2022. 33(32): p. 24397-24433; https://doi.org/10.1007/s10854-022-09204-7

[7] Cheng, C.-C., et al., RSC Advances, 2018. 8(46): p. 26341-26348; https://doi.org/10.1039/C8RA04968H

[8] Chen, C.-C., et al., Sensors and Materials, 2019. 31(3): p. 1083-1089; https://doi.org/10.18494/SAM.2019.2228

[9] ElFaham, M.M., A.M. Mostafa, E.A. Mwafy, Journal of Physics and Chemistry of Solids, 2021. 154: p. 110089; https://doi.org/10.1016/j.jpcs.2021.110089

[10] Bayda, S., et al., Molecules, 2019. 25(1): p. 112; https://doi.org/10.3390/molecules25010112

[11] Cui, Q., et al., Journal of the Taiwan Institute of Chemical Engineers, 2023. 142: p. 104679; https://doi.org/10.1016/j.jtice.2023.104679

[12] Sarkar, S., A.D. Mahapatra, D. Basak, Journal of colloid and interface science, 2018. 523: p. 245-253; https://doi.org/10.1016/j.jcis.2018.03.110